Supplementary Materials for

Cell membranes resist flow

Zheng Shi[1,4], Zachary T. Graber[2], Tobias Baumgart[2], Howard A. Stone[3], Adam E. Cohen[1,4]*
[1]Department of Chemistry and Chemical Biology, Harvard University.
[2]Department of Chemistry, University of Pennsylvania.
[3] Department of Mechanical and Aerospace Engineering, Princeton University.
[4] Howard Hughes Medical Institute.

*Correspondence to: cohen@chemistry.harvard.edu

This PDF file includes:

Materials and Methods

Cell culture, transfection, and staining

Henrietta Lacks (HeLa) cells, NIH/3T3 fibroblasts, and Madin–Darby canine kidney (MDCK) epithelial cells were cultured following standard protocols. Briefly, cells were grown in DMEM supplemented with 10% FBS and penicillin/streptomycin in a 37 °C incubator under 5% CO_2. Cells were grown to 50-70% confluence in 3.5 cm dishes and transfected with 0.5 - 1 μg desired plasmid using TransIT-X2 (Mirus MIR6003). One day after transfection, cells were trypsinized and re-plated at a density of 10,000 - 30,000 cells/cm^2 on glass-bottom dishes. Experiments were performed the following day. Before imaging, the cell culture medium was replaced with extracellular (XC) imaging buffer (125 mM NaCl, 2.5 mM KCl, 15 mM Hepes, 30 mM glucose, 1 mM $MgCl_2$, 3 mM $CaCl_2$, and pH 7.3). All lipids were purchased from Avanti Polar Lipids. Texas Red® DHPE was from Life Technologies.

All procedures involving animals were in accordance with the National Institutes of Health Guide for the care and use of laboratory animals and were approved by the Institutional Animal Care and Use Committee (IACUC) at Harvard. Hippocampal neurons from P0 rat pups were dissected and cultured in NBActiv4 medium at a density of 30,000 cells/cm^2 on glass-bottom dishes pre-coated with poly-d-lysine (Sigma P7205) and matrigel (BD biosciences 356234). At 1 day in vitro (DIV), glia cells were plated on top of the neurons at a density of 7000 cells/cm^2. At DIV5 - 7, neurons were transfected following the calcium phosphate protocol (Jiang and Chen, 2006). Imaging was performed 5 - 7 days after transfection, with neuron culture medium replaced with XC buffer.

Primary mouse brain endothelial (mBEC) cells were dissected and cultured in complete mouse endothelial cell medium (Cell Biologics M1168). For tether imaging or Ca^{2+} imaging, cells were plated at a density of 10,000 - 30,000 cells/cm^2 on glass-bottom dishes and stained with CellMask™ (Thermo Fisher C37608) for 10 minutes or with Fluo-4-AM (Life Technologies F14201) for 30 min before experiments. For vesicle imaging, cells were grown to 50% confluence in 3.5 cm dishes and transfected with lenti-virus encoding mOrange2-TM. 5 - 7 days after transfection, cells were trypsinized and re-plated at a density of 10,000 - 30,000 cells/cm^2 on glass-bottom dishes. Experiments were performed 12 – 36 hours after cells were plated to glass-bottom dishes. Before imaging, the cell culture medium was replaced with XC buffer. Neurons and mBEC cells were fed twice weekly until experiments.

For nonspecific extracellular staining of transmembrane proteins, cells were incubated with 250 μg/mL Alexa Fluor™ 488 NHS Ester (Thermo Fisher A20000, dissolved using the original cell culture medium) for 30 minutes. Cells were then washed 3 - 5 times with 1 mL XC buffer before imaging. Amaranth (Sigma 87612), with a final concentration of 500 μM, was used to quench the Alexa488 fluorescence.

For imaging intracellular vesicles with FM 4-64 (Thermo-Fisher T13320), cells were incubated with 20 μg/mL FM 4-64 for 20 minutes. Cells were then washed 5 times with 1 mL XC buffer before imaging, leaving the cell with only intracellular vesicles stained. Fusion of vesicles was reported as the disappearance of fluorescent puncta (Gauthier et al., 2009). Ionomycin (Sigma I9657), with a final concentration of 5 μM, was used to trigger cell-wide vesicle fusion.

DNA constructs

All constructs used in this study are described in Table S2. pCAG: GPI-eGFP (Addgene plasmid # 32601, eGFP targeted to the plasma membrane using the glycophosphatidylinositol anchor) was a gift from Anna-Katerina Hadjantonakis (Rhee et al., 2006). mOrange2-KRAS: mOrange2 targeted to the inner leaflet of plasma membrane using the C-terminus sequence of KRAS. Lifeact-CFP was a gift from Bo Zeng (Zeng et al., 2017). DRD2-eGFP: dopamine receptor D2 with eGFP. CheRiff-eGFP: an ultra-sensitive, fast, and well trafficked channelrhodopsin variant linked with eGFP (Hochbaum et al., 2014). ASAP1: Accelerated Sensor of Action Potentials 1 (St-Pierre et al., 2014). eGFP-TM: eGFP targeted to the extracellular side of the plasma membrane, using a transmembrane helix from PDGF receptor on the pDisplay^{TM} Mammalian Expression Vector (Thermo Fisher). eGFP-KRAS: eGFP targeted to the inner leaflet of plasma membrane using the C-terminus sequence of KRAS. R-CaMP2 was a gift from Haruhiko Bito (Inoue et al., 2015). GCaMP6f (Addgene plasmid # 40755) was a gift from Douglas Kim (Chen et al., 2013). PIEZO1-mCherry was a gift from Ardem Patapoutian. mOrange2-TM: mOrange2 targeted to the extracellular side of the plasma membrane, using a transmembrane helix from PDGF receptor on the pDisplay^{TM} Mammalian Expression Vector.

Bleb formation

Blebs were induced by treating the cells grown on glass bottom dish with 100 - 200 μM latrunculin B (Sigma L5288) dissolved in 200 μL XC buffer. Blebs started forming within 3 minutes of drug addition. Then, 2 mL of XC buffer was added to the dish and majority of the blebs became stable for further experiments.

Glass micropipette fabrication, tether pulling, and imaging

Micropipettes were pulled from glass capillaries (WPI 1B150F-4) using a pipette puller (Sutter Instrument P1000). The tip of the pipette was cut to an opening diameter of ~3 μm and bent to ~40° using a microforge (WPI DMF1000). Experiments were performed on a home-built epi-fluorescence microscope (Kralj et al., 2011). Two Sutter manipulators (Sutter Instrument MP-285) controlled pipette motion.

The pipettes were immersed in a dispersion of 4 μm diameter Anti-Digoxigenin coated polystyrene beads (Spherotech DIGP-40-2), and suction was applied to plug each pipette aperture with a single bead. The beads were then brought into contact with cell membranes and retracted to pull out membrane tethers. A digital micromirror device (DMD) with 608 × 684 pixels (Texas Instruments LightCrafter) patterned the illumination to confine fluorescence excitation to the tether regions. In cases where tethers broke, the piece of tether attached to cells retracted to its mother cell within one minute. To obtain large membrane tension changes on blebs through tether pulling, it is advantageous to choose more spherical blebs. Otherwise, on floppy blebs, a change of tether length for ~ 100 μm does not result in measurable changes in tether fluorescence (or equivalently, membrane tension).

Measurements of tension-dependent tether pulling force on GUVs (Fig. S1) were performed on a home-built optical trap with 6 μm diameter streptavidin coated beads (Polysciences, Inc) as described previously (Heinrich et al., 2010; Shi and Baumgart, 2015).

Calibration between tether pulling force and tether intensity (with HeLa cells, as shown in Fig. S2C and S2D) was achieved with simultaneous recording of pulling force (through the optical trap) and tether fluorescence (with patterned illumination).

Tether diameters were estimated by imaging HeLa cells expressing membrane-bound fluorescent proteins. By measuring the cumulative fluorescence I_{cell} in a patch of flat cell membrane of area A_{cell} and the cumulative fluorescence I_{tether} on tethers (pulled from the same cell) of length l (Fig. S2B), the diameter of a single tether is calculated using:

$$d_{tether} = \frac{2I_{tether}A_{cell}}{\pi I_{cell} l}.$$

The factor of 2 in the numerator accounts for the fact that the cell has top and bottom membranes, both of which contribute to I_{cell}. All experiments with cells were performed with a 60x oil objective (Olympus UIS 2, N.A. 1.49) with an objective heater (Bioptechs) to keep the sample at 37 °C.

Fluorescence recovery after photobleaching (FRAP) measurements of diffusion

To measure tracer diffusion on cell membranes, a flat patch of membrane was photobleached within a circular region of radius r = 7 μm at an illumination intensity of 1 kW/cm^2 for ~ 60 s. Then an illumination intensity of 0.5 W/cm^2 was used to monitor the recovery. To measure tracer diffusion on tethers, the same laser spot was used to bleach a d = 14 μm long region of tether. Measurements on plasma membrane and tether were performed sequentially on the same cells.

For FRAP measurements on the cell, the fluorescence recover was fit to the relation:

$$I(t) = \frac{I_0 + I_\infty \frac{t}{\tau_{0.5}}}{1 + \frac{t}{\tau_{0.5}}}.$$

The diffusion coefficient was extracted using (Kang et al., 2012) $D_s{}^{cell} = \frac{r^2}{4\tau_{0.5}}$.

For FRAP measurements on the tether, the recovery phase was fit to:

$$I(t) = I_\infty - I_0 \exp(-t/\tau_{exp}).$$

The diffusion coefficient was extracted using (Rosholm et al., 2017) $D_s{}^{tether} = \frac{4d^2}{\pi^2 \tau_{exp}}$. The high membrane curvature in tethers is reported to slightly decrease diffusion relative to a planar bilayer (by less than a factor of 2) (Domanov et al., 2011), an effect that we neglected.

FRAP measurement of fraction of transmembrane proteins that are immobile

To measure the immobile fraction of cell surface proteins, NHS-ester Alexa 488 labeled cells were bleached with a donut shape laser beam (inner radius 17.5 μm, outer radius 35 μm) following the procedure described above.

The immobile fraction of proteins was calculated using

$$\frac{\phi_i}{\phi_t} = \frac{I^{end}_{center} - I^{end}_{ring}}{I^{0}_{center} - I^{0}_{ring}}.$$

Here, the ϕ_t represents the area fraction of all labeled transmembrane proteins. I^0_{center} and I^0_{ring} represent fluorescence intensities right after photobleaching in unbleached and bleached regions respectively (at t ~ 100 s, see Fig. S6C). I^{end}_{center} and I^{end}_{ring} represent fluorescence

intensities, in unbleached and bleached regions respectively, at the end of the FRAP experiment (t = 1000 s).

Simulation of relaxation of membrane tension in a tether

To model tension relaxation in a pulled tether, we decomposed the experiment into three steps:

(I) *Initial equilibrium*

Tether length l, radius r and membrane tension, σ, are related by:

$$A = 2\pi r l,$$
$$\sigma = \frac{\kappa}{2r^2}.$$

Here, A is the tether surface area; κ is the bending stiffness of the membrane.

Combining these two relations leads to an expression for membrane tension as a function of tether length and area:

$$\sigma(A, l) = \frac{2\pi^2 \kappa l^2}{A^2}.$$

(II) *Elongation of tether at constant velocity,* v_{pull}

The simulation is broken into small time-steps of length Δt = 3 s. For each time-step, the dynamics are described by three processes:

1: At constant tether area, A, increase tether length by $\Delta l = v_{pull}\Delta t$. Then update l, r, and σ, without allowing flow of lipids from the cell into the tether:

$$l \to l + \Delta l,$$
$$r = \frac{A}{2\pi l},$$
$$\sigma \to \sigma + \frac{4\pi^2 \kappa}{A^2} l \Delta l.$$

2: Calculate the diffusion of tension in the cell membrane, treating the membrane as a 20 μm radius disk and matching tension across the cell-tether boundary at radius r:

$$\frac{\partial \sigma}{\partial t} = D_\sigma \nabla^2 \sigma.$$

3: Calculate flow of lipids from the cell membrane into the tether, keeping l constant. The flux into the tether is given by the solution to the tension diffusion equation at the cell-tether boundary:

$$\Delta A = 2\pi r \frac{k \nabla \sigma}{\eta} \Delta t$$
$$A \to A + \Delta A,$$
$$\sigma \to \sigma - \frac{4\pi^2 \kappa l^2}{A^3} \Delta A.$$

(III) *Relaxation of tension via lipid flow into a tether of constant length*

The steps are the same as in (II) except that tether length is always kept constant. The results of these simulations are plotted in Fig. 2F.

Tether pulling and Ca^{2+} imaging

For simultaneous imaging of tethers and Ca^{2+} influx, MDCK cells were co-transfected with GPI-eGFP and R-CaMP2. Blue laser light (488 nm) for exciting GPI-eGFP was confined to the tether region via a digital micromirror device, while green laser light (532 nm) for exciting R-CaMP2 illuminated the whole cell (Fig. 3B). Images were acquired continuously at 5 Hz with an emission filter simultaneously passing GFP and RFP emission wavelengths. Initiation points of Ca^{2+} influx were determined as the center of the Ca^{2+} influx (as shown in the heat map of Fig. 3C) in its first observable frame.

In the studies of the effects of Gd^{3+} (Sigma 203289-1G) and GsMTx4 (Tocris 4912, Fig. 3D) on Ca^{2+} influx, MDCK cells were transfected with GCaMP6f as a Ca^{2+} reporter. Under wide-field 488 nm excitation, images were acquired continuously at 2 Hz with an emission filter for GFP.

In the study of the effect of PIEZO1 on Ca^{2+} influx, MDCK cells were co-transfected with PIEZO1-mCherry and GCaMP6f. PIEZO1-mCherry expressing cells were identified with 532 nm excitation and an emission filter for RFP. Images were acquired continuously at 2 Hz under wide-field 488 nm excitation with an emission filter for GFP.

All tether pulling experiments shown in Fig. 3D and 3I followed the same tether pulling protocol (move the bead to gently touch a GCaMP6f expressing cell for 20 s, then pull bead away from the cell for 500 μm with the first 200 μm at 5 μm/s and the next 300 μm at 10 μm/s). Changes of GCaMP6f fluorescence (F_{max}/F_0) were measured in the region of bead-cell attachment (diameter 4 μm circle) with corrections for background and photo bleaching. F_{max} is the peak fluorescence during tether elongation; F_0 is the fluorescence baseline before tether pulling. We poked holes on the cells at the end of each tether pulling experiment to verify that the cells could report Ca^{2+} influx. In mBEC cells, the same tether pulling protocol was applied to cells stained with Fluo-4-AM (Fig. 4A).

Tether pulling and vesicle fusion

The same tether pulling protocol used for MSC activation and Ca^{2+} imaging was applied to cells expressing mOrange2-TM (Fig. 3G and 4B). Under wide-field 532 nm excitation, images were acquired continuously at 1 Hz with a 562/40 nm bandpass filter. Vesicle fusion sites were determined as the center of bright dots that appeared during pulling (as shown in the heat map of Fig. 3G and 4B).

To determine the distribution of tether-vesicle distances expected from the null hypothesis (vesicles fuse at random locations in the cell), the image of each cell was converted into a binary mask. The mean distance from the tether location to all points on the cell was then calculated. This distance was averaged over all cells measured.

In the study of the effect of 2-APB (Tocris 1224, Fig. 4D) on vesicle fusion in mBEC cells, mOrange2-TM transfected cells were incubated with 100 μM 2-APB in cell culture medium for 1 hour to deplete ER Ca^{2+} stores. The medium was then replaced with XC buffer for imaging.

Local flow experiments with mBEC cells

mBEC cells were stained with Fluo-4-AM or transfected with mOrange2-TM as described above. Pipettes with an exit diameter of R_p = 12 μm were used to inject XC buffer near one end of the cell by quickly increasing the pressure inside pipette. Fluorescence images were

acquired at 2 Hz. The flow speed was calibrated by measuring the rate of decrease of buffer volume in the pipette. For data shown in the main text, this rate was Γ = 14 nL/s. Buffer speed exiting pipette was calculated by $v_{flow} = \Gamma/(\pi R_p^2)$ = 12 cm/s. Maximal surface shear induced by the pipette was approximately $v_{flow}/R_p = 2\times10^4$ s^{-1}, corresponding to a surface stress of $\eta_c \cdot v_{flow}/R_p$ = 20 pN/μm^2. Here, $\eta_c = 10^{-3}$ Pa·s is the viscosity of XC buffer.

Supplementary Discussion

Relation between tether radius, pulling force, and membrane tension

For a tube of length l and radius r, the free energy of a tether U is (Brochard-Wyart et al., 2006; Derényi et al., 2002):

$$U = 2\pi r l\left(\frac{\kappa}{2r^2} + \sigma\right) - fl \qquad [S1]$$

Here κ is the bending stiffness of the membrane, σ is membrane tension, and f is the external pulling force.

The surface tension acts to reduce the radius (and therefore decrease the total area of the tether) while the bending stiffness works to increase the radius (to avoid membrane bending). The balance between these two forces sets the mechanical equilibrium. The equilibrium radius r_0 and pulling force f_0 are obtained from:

$$\frac{\partial U}{\partial r} = 2\pi l\left(-\frac{\kappa}{2r^2} + \sigma\right) = 0$$

and

$$\frac{\partial U}{\partial l} = 2\pi r\left(\frac{\kappa}{2r^2} + \sigma\right) - f = 0$$

from which we obtain:

$$r_0 = \sqrt{\frac{\kappa}{2\sigma}} \qquad [S2]$$

and

$$f_0 = 2\pi\sqrt{2\kappa\sigma} \qquad [S3]$$

These equations show that one can determine the tension of a bilayer by measuring either the tether radius or the pulling force.

Hydrodynamics of lipid flow

To describe lipid flow through a medium comprised of randomly dispersed immobile obstacles, the Stokes equation is augmented with a drag term (Bussell et al., 1995; Howells, 1974) $\frac{\eta}{k}\vec{v}$:

$$\nabla\sigma = -\eta\nabla^2\vec{v} + \frac{\eta}{k}\vec{v} \qquad [S4]$$

where σ is the membrane tension, η is the two-dimensional membrane viscosity, $\vec{v}$ is the velocity field of lipid flow, and k is the Darcy permeability of the array of obstacles. When the Brinkman equation is written for pressure, rather than membrane tension, the signs on the right-hand side are reversed (fluids flow from high to low pressure, but membranes flow from low to high tension). Physically, the ratio $\frac{\eta}{k}$ is the drag coefficient of a fixed array of obstacles.

Conservation of mass requires that:

$$\frac{\partial \rho}{\partial t} + \nabla \cdot (\rho \vec{v}) = 0 \quad [S5]$$

where ρ is the two-dimensional density of lipids. Assuming a small perturbation to lipid density, $\rho = \rho_o + \delta\rho$, Eq. S5 becomes:

$$\frac{\partial \rho}{\partial t} = -\rho_o \nabla \cdot \vec{v} \quad [S6]$$

We assume a linear stress-strain relation for the membrane tension (Hochmuth et al., 1973):

$$\delta\sigma = -E_m \, \delta\rho/\rho_o \quad [S7]$$

where E_m is the effective area expansion modulus of the cell membrane. Equations S4, S6, and S7 describe the hydrodynamics of lipid flow in cell membranes containing random arrays of fixed obstacles. The equations can be combined to obtain:

$$\frac{E_m}{\eta}\nabla^2\sigma = \left(-\nabla^2 + \frac{1}{k}\right)\frac{\partial \sigma}{\partial t} \quad [S8]$$

Neglect of membrane obstacles is equivalent to keeping only the first term on the right-hand side of Eq. S4 or S8.

$$\frac{\partial \nabla^2\sigma}{\partial t} = -\frac{E_m}{\eta}\nabla^2\sigma \quad [S9]$$

This relation identifies a relaxation time for tension fluctuations, $\tau = \eta/E_m$. Inserting estimates of membrane viscosity (η = (3.0 ± 0.4) × 10^{-3} pN·s/μm) and area expansion modulus (E_m = 40 pN/μm)(Hochmuth, 2000) gives a relaxation time less than 0.1 ms, as has been used in the literature (Keren et al., 2008).

If the spacing between transmembrane obstacles is small compared to externally imposed variations in the flow field, then the second term of Eq. S4 or S8 dominates, and we obtain a diffusion-like equation for membrane tension:

$$\frac{\partial \sigma}{\partial t} = D_\sigma \nabla^2 \sigma \quad [S10]$$

with

$$D_\sigma = \frac{E_m k}{\eta}. \quad [S11]$$

In other words, if l_c is a characteristic length scale of variations in σ then Eq. S10 applies when $\frac{k}{l_c^2} \ll 1$. The same result describes the three-dimensional propagation of pressure in a porous elastic medium (Charras et al., 2005).

Calculation of drag due to a random array of fixed cylinders

When N_i immobile proteins are present in a piece of membrane with area A, the immobile area fraction is $\phi_i = \frac{N_i \pi a^2}{A}$, where a is the radius of one immobile particle. Bussel *et al.*(Bussell et al., 1995) adapted Howell's mean-field solution of the Stokes equation for a random array of cylindrical obstacles (Howells, 1974) to calculate the mean force, $\vec{F}_0$, required to drag one particle with a mean velocity $\vec{U}$ through the background of immobile particles.

We introduce the dimensionless quantity $x = \frac{a}{k^{1/2}}$, where a is the radius of an obstacle and k is the Darcy permeability coefficient. Then:

$$\vec{F}_0 = \frac{\vec{U}}{m_b} = 4\pi\eta\left(\frac{x^2}{2} + \frac{xK_1(x)}{K_0(x)}\right)\vec{U} \quad [S12]$$

Here, m_b is the mobility of the tracer particle, and K_0 and K_1 are the modified Bessel functions of the second kind with orders of 0 and 1, respectively.

According to the Brinkmann model, the mean force per unit area to drag the membrane at velocity $\vec{U}$ is:

$$\frac{\phi_i}{\pi a^2}\vec{F}_0 = \frac{\eta}{k}\vec{U} \quad [S13]$$

Together, these two equations lead to the relation between permeability and immobile protein fraction:

$$\phi_i = \frac{x}{2x+4\frac{K_1(x)}{K_0(x)}} \quad [S14]$$

The dimensionless diffusion coefficient of tracer molecules is related to the mobility via:

$$\frac{\pi\eta D_s}{k_B T} = \pi\eta m_b = \frac{1}{2x^2+4x\frac{K_1(x)}{K_0(x)}} \quad [S15]$$

The dimensionless diffusion coefficient of membrane tension is:

$$\frac{\eta D_\sigma}{E_m a^2} = \frac{k}{a^2} = \frac{1}{x^2} \quad [S16]$$

The upper limit of tracer diffusion is given by the Saffman–Delbrück model (Saffman and Delbrück, 1975):

$$\frac{\pi\eta {D_s}^{max}}{k_B T} = \frac{1}{4}\left[\ln\left(\frac{\eta}{\eta_c a}\right) - 0.577\right] \quad [S17]$$

where η_c is the viscosity of the fluid medium surrounding the membrane and it is assumed that $\frac{\eta}{\eta_c a} \gg 1$.

For diffusion of tension, hydrodynamic coupling to the cytoskeleton exerts viscous drag even in the absence of fixed obstacles. This drag sets an upper bound on the diffusion coefficient for membrane tension:

$$\frac{\eta {D_\sigma}^{max}}{E_m a^2} = \frac{\eta h}{\eta_c a^2} \quad [S18]$$

where h is the distance between the cortical cytoskeleton and the plasma membrane (see Fig. 2). We used $\eta_c = 10^{-3}$ pN·s/μm^2, a = 2 nm (Bussell et al., 1995), and h = 20 nm (Clausen et al., 2017).

Equation of state of membranes

The relation between the projected membrane density and the membrane tension is given in equation [S7]. The resting tension of the cell membrane (~25 pN/μm) is much lower than the tension where enthalpic stretching of lipid bilayers becomes significant (500 pN/μm) (Evans and Rawicz, 1990). Microscopically, the membrane has undulations due to thermal fluctuations, due to fluctuations in the underlying cytoskeletal support, and possibly due to binding of curvature-inducing proteins (Shen et al.) (e.g. in caveolae). The membrane density, ρ_0, refers to a projected density of lipids after averaging over these microscopic undulations. Tension can partially smooth these undulations, leading to an effective stretching modulus that does not involve changing the mean spacing between lipid molecules. Experimental measurements of the effective area expansion modulus of cells (Hochmuth, 2000) indicate that the apparent elasticity is mainly associated with structures such caveolae and microvilli

and the contribution from thermal agitation is negligible (Evans and Rawicz, 1990; Hochmuth et al., 1973; Hochmuth, 2000).

Supplementary Figures

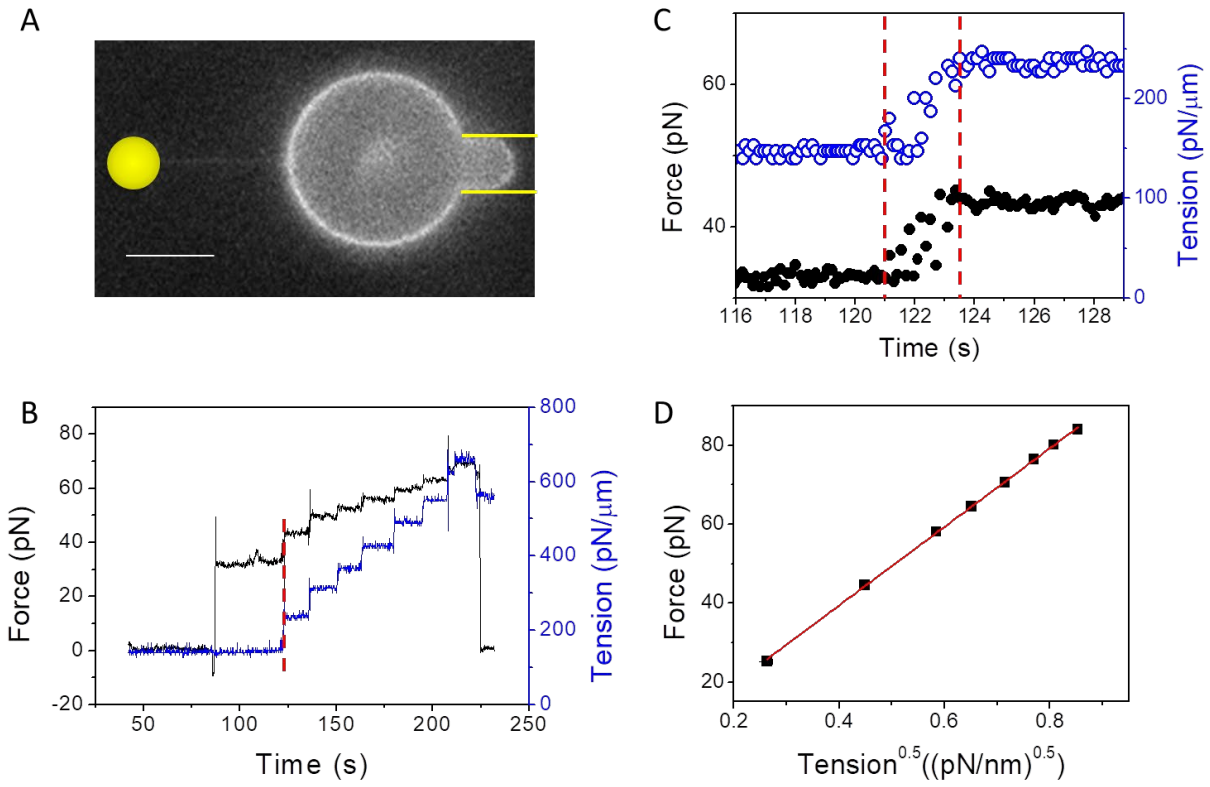

Fig. S1. Membrane tension equilibrates quickly in artificial lipid bilayers.
A) Fluorescence image of a micropipette-aspirated GUV (DOPS:DOPE:DOPC = 35:30:35) containing 0.5% DSPE-Bio-PEG2000 and labeled with 0.3% Texas Red® DHPE. The edge of the pipette is marked with yellow lines. An optically trapped bead (position indicated by the yellow circle) pulled a membrane tether opposite to the pipette. Scale bar 10 μm. **B)** Changes in membrane tension (blue) were induced by applying steps of pressure to the pipette and tether pulling force (black) was monitored via the optical trap. **C)** Close-up of the step marked with a red line in **B**, showing no detectable delay between change in tension and change in tether force. Measurements sampled at 10 Hz. **D)** Relation between tether pulling force and the square root of membrane tension, with a linear fit following the relation: $f = 2\pi\sqrt{2\kappa\sigma}$ (red line, $R^2 = 0.99$). Error bars are s.e.m..

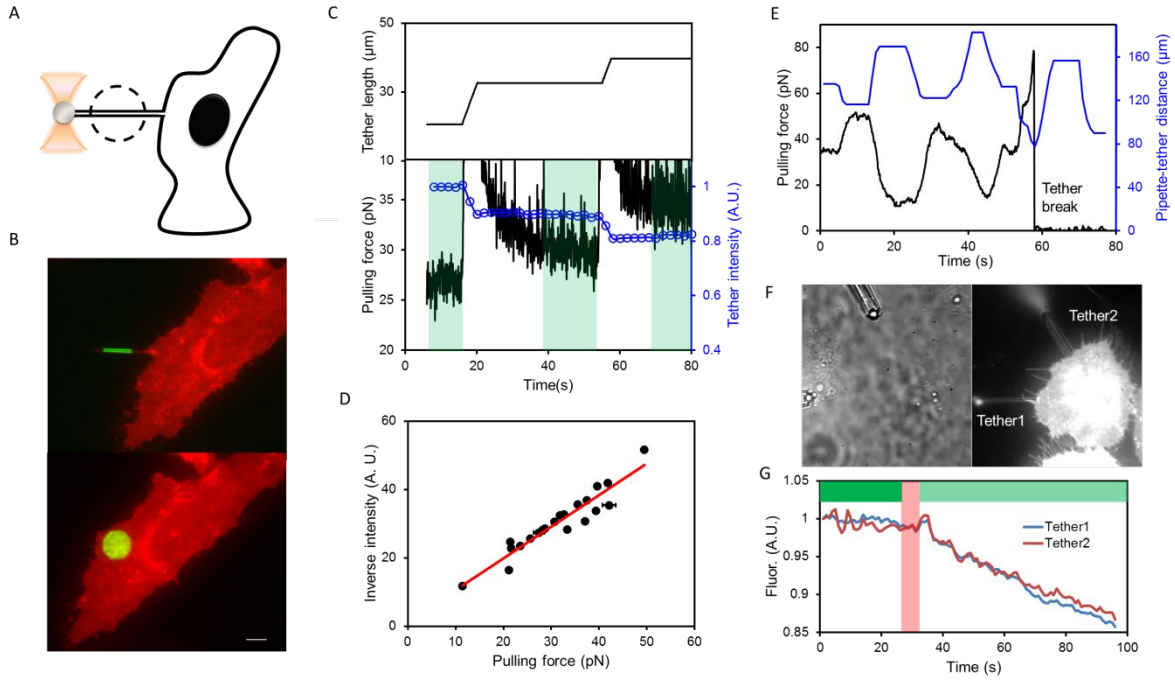

Fig. S2. Tether diameter reports membrane tension.

A) Schematic showing simultaneous measurement of tether pulling force (with an optical trap) and tether fluorescence intensity (with patterned illumination in the dashed circle). **B)** Determination of tether diameter from tether fluorescence intensity. A 14 μm diameter circular spot of illumination was first directed to a tether (top) and then to a flat portion of the parent cell (bottom). The ratio of the total fluorescence excited in these two configurations equals the ratio of illuminated membrane areas. These calibrations yielded an average tether diameter d_{tether} = 150 ± 10 nm (mean ± s.e.m., n = 5 cells) for tethers ~ 20 μm long. Measured average tether pulling force was f_{tether} = 16 ± 1 pN (mean ± s.e.m., n = 10 cells), leading to a membrane bending stiffness $\kappa = (1.9 \pm 0.2) \times 10^{-19}$ J. Scale bar, 10 μm. **C)** Tethers were pulled with a bead in an optical trap, and tether length, fluorescence intensity, and force were measured simultaneously. Regions shaded in green were used to calculate the relation between steady state tether fluorescence intensity and pulling force. **D)** Relation between tether pulling force and inverse of tether fluorescence intensity (normalized to expression level; R^2 = 0.9, n = 7 cells). Error bars are s.e.m. **E)** Perturbation to membrane tension via osmotic shocks. Tether pulling force was measured with an optical trap while a pipette flowed pure water over the cell. As the pipette approached the cell, the pulling force increased, signaling an increase in membrane tension. As the pipette withdrew, the tension decreased. **F)** Transmitted light (left) and fluorescence (right) images showing two sets of tethers pulled from the same cell. **G)** Response of tether fluorescence to gradual addition of hypotonic buffer (20 mOsm buffer added to equal volume of 300 mOsm XC buffer during time shaded in red). Experiments were performed at 37 °C on HeLa cells expressing membrane-targeted fluorescent protein mOrange2-KRAS (**A** – **E**) and GPI-eGFP (**F**, **G**).

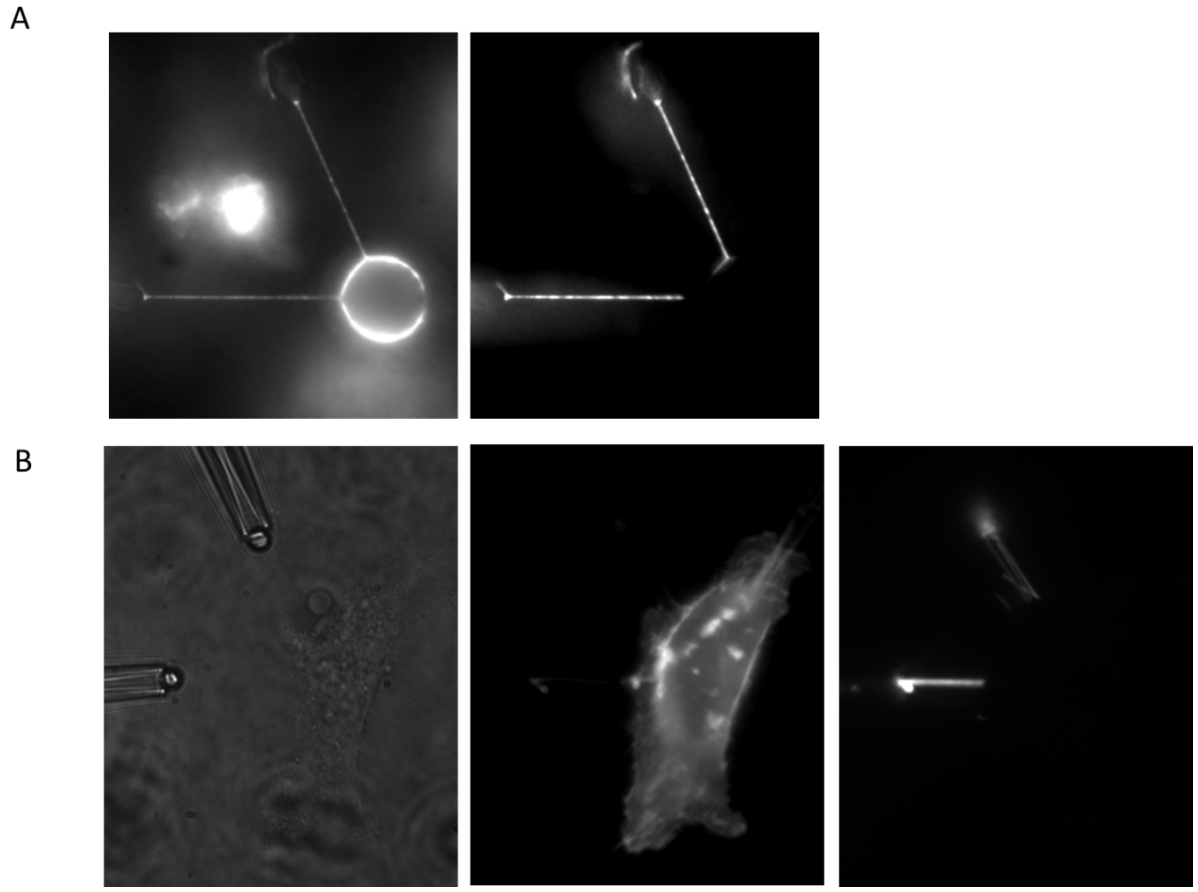

Fig. S3. Non-composite images of Fig. 1A and Fig. 1D.

A) Left: Wide-field epifluorescence image of a bleb in a HeLa cell expressing GPI-eGFP with two tethers. Right: Same structure, with patterned illumination restricted to illuminating the tethers. **B)** Left: Transmitted light image of two pipettes with polystyrene beads at the ends. Middle: Wide-field epifluorescence image of a HeLa cell expressing GPI-eGFP. Right: Same structure, with patterned illumination restricted to illuminating the tethers.

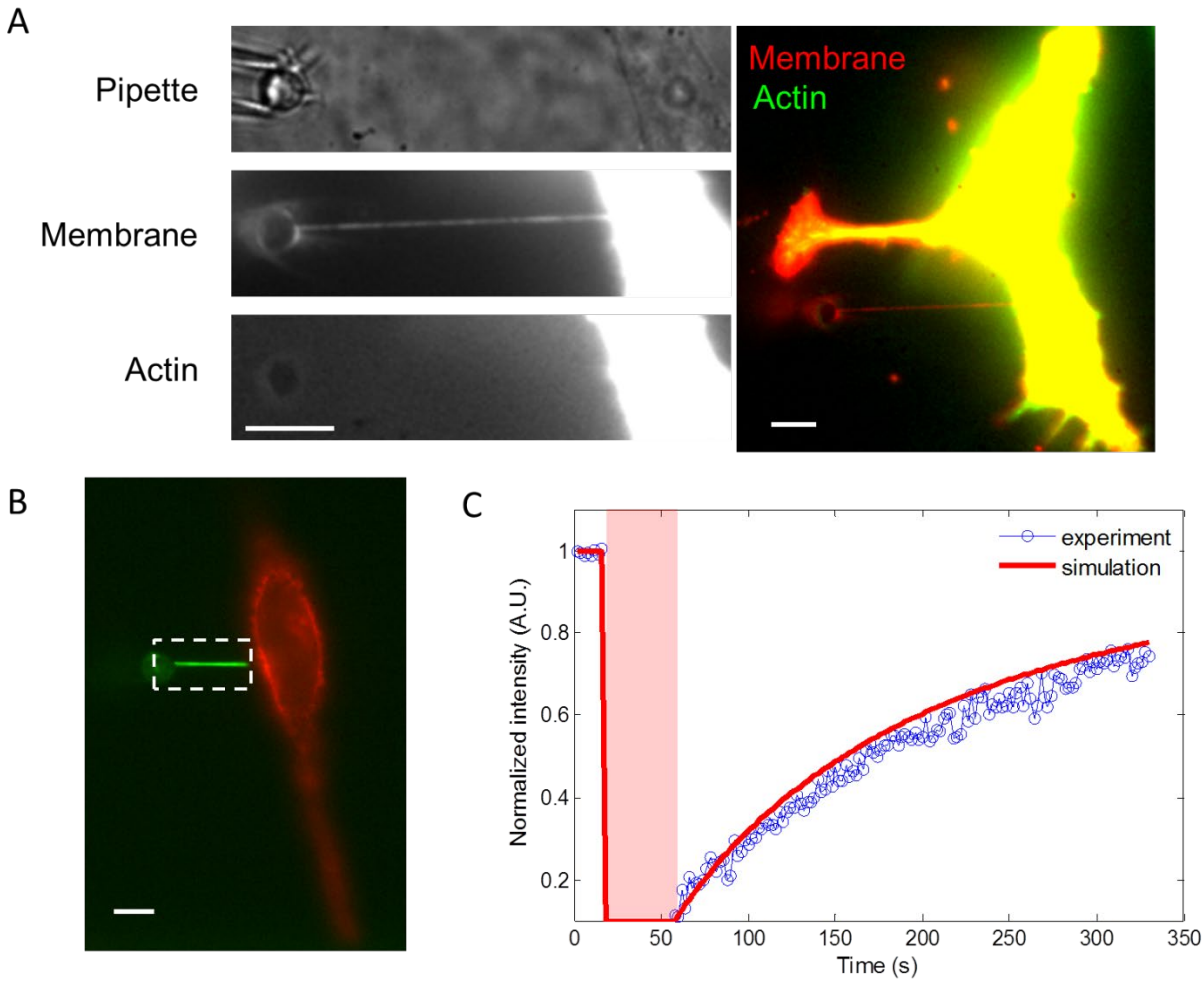

Fig. S4. Tethers are in diffusive contact with the plasma membrane.

A) Actin cytoskeleton does not penetrate membrane tethers. Top left: transmitted light image showing position of the tether pulling pipette. Middle and bottom left: Simultaneous images of cell membrane (mOrange2-KRAS) and actin (Lifeact-CFP) in a tether. Images were taken 15 min after tether formation. Right: Composite image of the whole cell. Red: membrane, green: actin. **B)** FRAP experiment to test whether tether and cell membrane are in diffusive equilibrium. Composite fluorescence image showing the photobleached region (dashed box) on a tether (green), attached to a HeLa cell (red) expressing DRD2-eGFP **C)** FRAP of the tether (blue) and corresponding simulation (red) assuming free diffusion from cell to tether. The simulation used the experimentally measured diffusion coefficient of DRD2-eGFP on the cell, D_s(Cell) = 0.037 μm^2/s (see Table S2), and a tether radius of 75 nm. Since D_s(Cell) << D_s(Tether), the smaller diffusion coefficient dominated the transport and was the appropriate choice for the simulations. The simulation was performed in Matlab. Time of photobleaching is shaded red. Scale bars in all panels 10 μm.

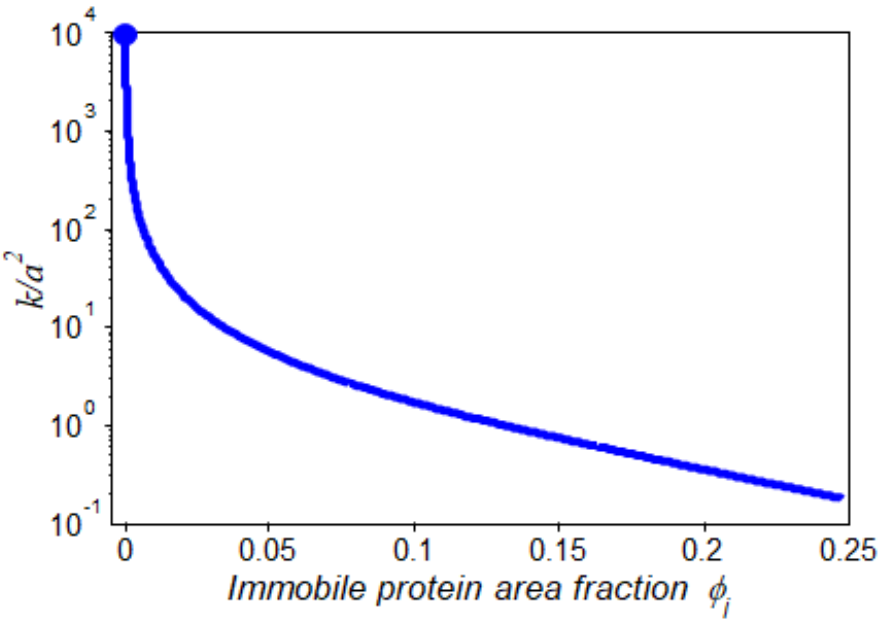

Fig. S5. Relation between Darcy permeability *k* and area fraction of immobile proteins ϕ_i.

The function $\frac{k}{a^2} = f(\phi_i)$ was derived by Bussell (Bussell et al., 1995) *et al.*, who showed that $\phi_i = \frac{x}{2x+4\frac{K_1(x)}{K_0(x)}}$, where $x = \frac{a}{k^{1/2}}$ (see *Supplementary Discussion*). The upper limit (blue dot) is calculated from viscous drag of the cytoplasm layer between membrane and actomyosin cortex

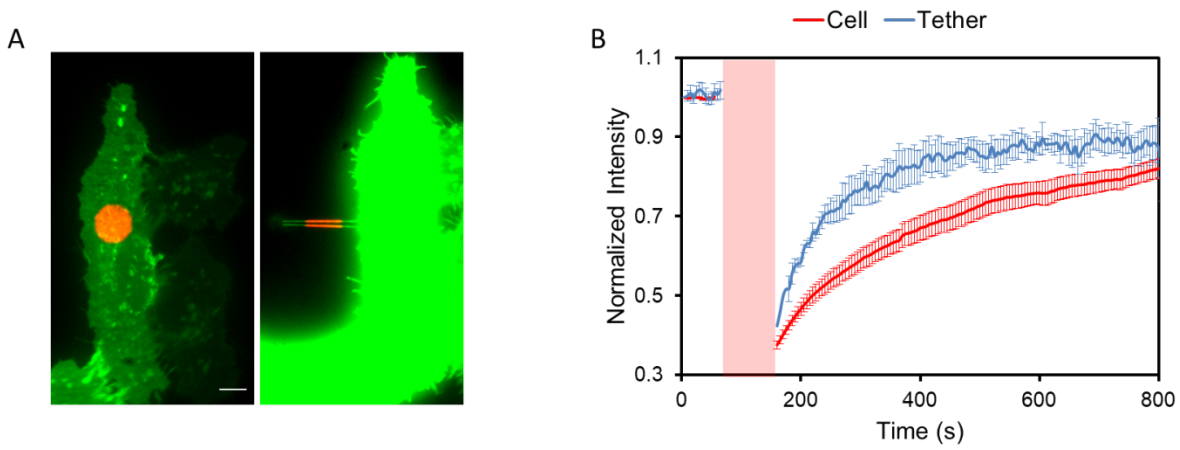

Fig. S6. FRAP measurements of tracer diffusion on cell membranes and on tethers.

A) Composite images showing the cell (green) and 14 μm circular photobleaching spot (red). Left: FRAP on cell membrane. Right: FRAP on tether. Scale bar, 10 μm. **B)** FRAP data in HeLa cells expressing DRD2-eGFP. Error bars represent s.e.m. from n = 10 tethers pulled from 10 cells. Time of photobleaching is shaded red.

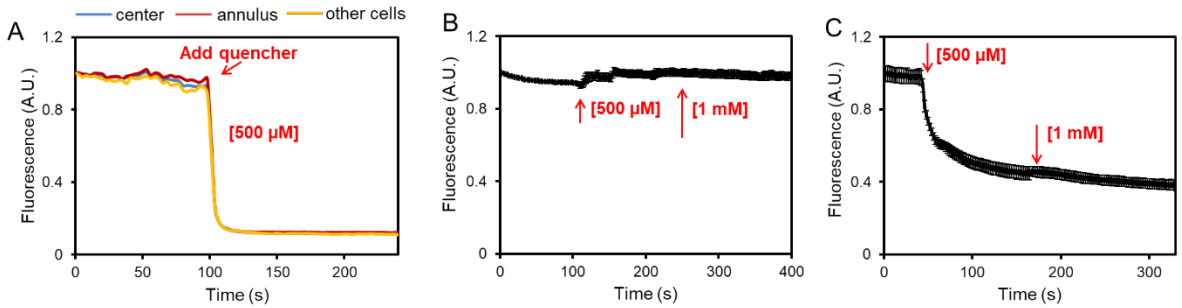

Fig. S7. Validation of FRAP measurement of the immobile fraction of transmembrane proteins.

A) After the FRAP measurement as shown in Fig. 2E, a cell impermeant fluorescent quencher, amaranth, was added to a final concentration of 500 µM to quench the Alexa488 fluorescence. Fluorescence of all regions of the cell membrane dropped to background levels, establishing that there was no detectable internalization of fluorescently labeled proteins. **B-C)** Validation that amaranth functions as a cell-impermeant fluorescence quencher. **B)** In cells expressing, intracellular eGFP (eGFP-KRAS) amaranth did not affect fluorescence but **C)** in cells expressing extracellular eGFP (pDisplay: eGFP-TM) amaranth quenched fluorescence. Error bars are s.e.m. over $n = 4$ cells for eGFP-KRAS and $n = 5$ cells for eGFP-TM.

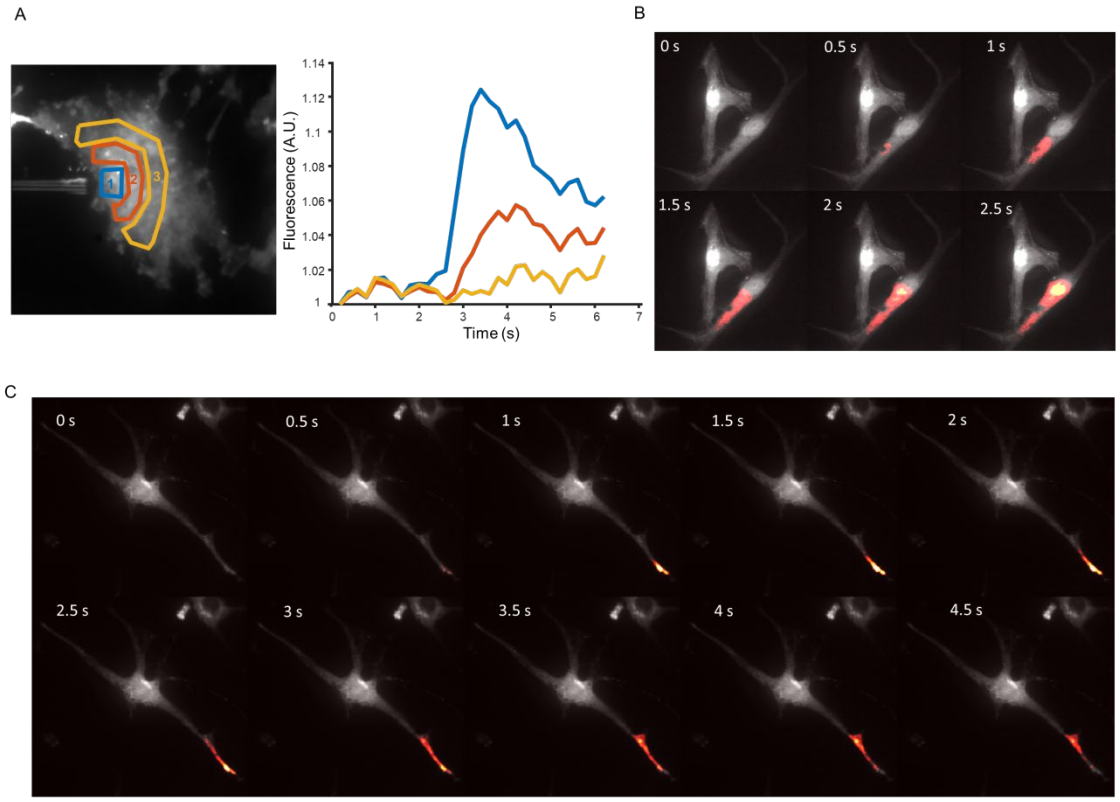

Fig. S8. Dynamics of Ca^{2+} entry through mechanosensitive ion channels. A) MDCK cell from Fig. 3C. Fluorescence of the R-CaMP2 reporter in different regions of interest as a function of time after initial Ca^{2+} influx. The dynamics show diffusion of Ca^{2+} from the point of tether attachment into the cell. **B)** mBEC cell from Fig. 4A. Filmstrip of fluorescence recordings in response to activation of mechanosensitive ion channels via tether pull. The movie shows local activation followed by intracellular spread of Ca^{2+}. **C)** mBEC cell of Fig. 4E. Fimstrip of fluorescence recordings in response to local shear flow. The Ca^{2+} influx starts at the region of maximum shear, followed by intracellular propagation of Ca^{2+}.

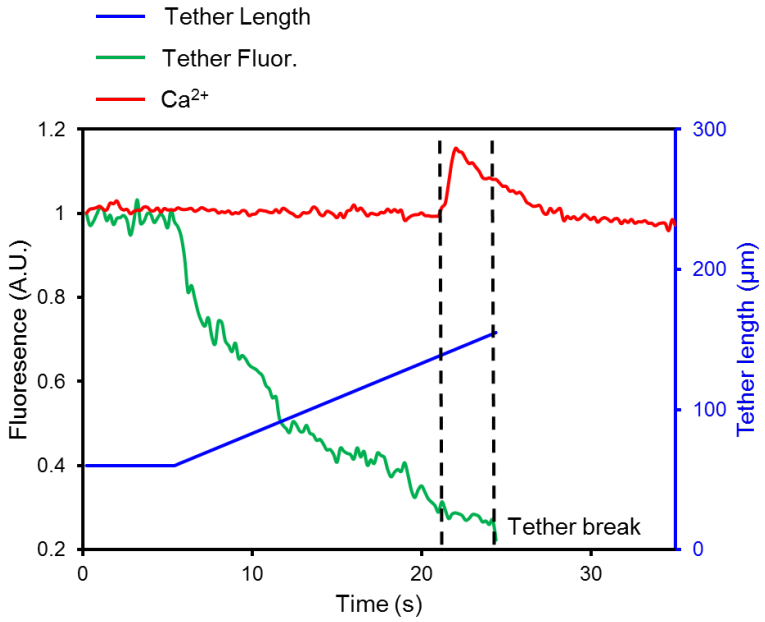

Fig. S9. Simultaneous imaging of tether fluorescence and intracellular Ca^{2+} during tether pulling experiments.

In experiments as shown in Fig. 3B, tether fluorescence intensity reports tether radius. Membrane tension can then be estimated from $\sigma = \frac{\kappa}{2{r_0}^2}$ (see *Supplementary Discussions*). The activation tension of MSCs was found to be approximately 11 times higher than the resting tension of the cell (dashed line, resting membrane tension is ~25 pN/µm). This estimate of activation tension is a lower bound because at the time of MSC activation the tether was still elongating, so tether diameter was not fully equilibrated.

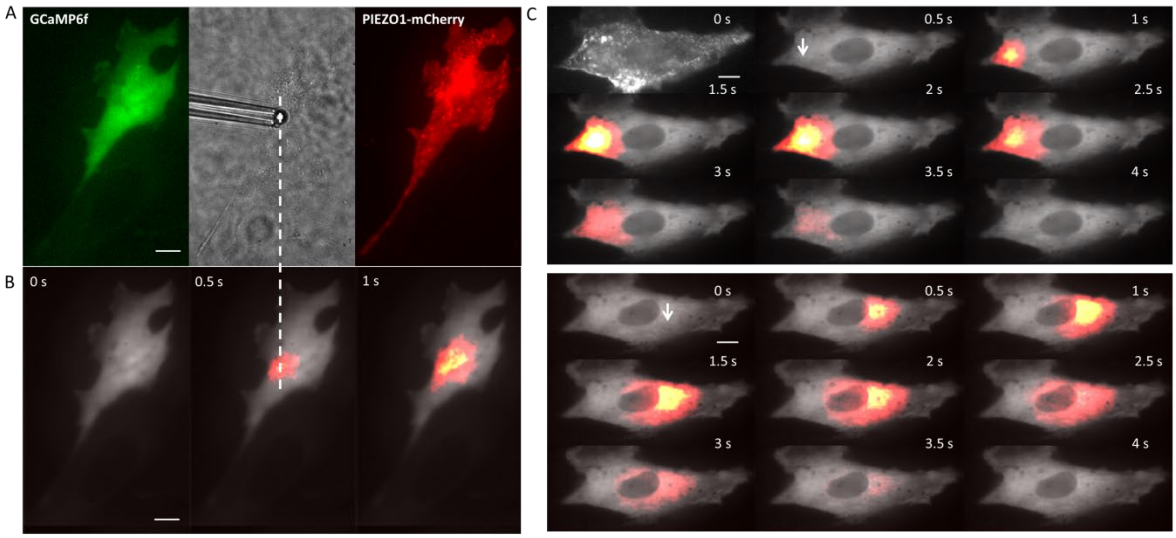

Fig. S10. Local activation of mechanosensitive ion channels in MDCK cells expressing PIEZO1-mCherry.

A) MDCK cell co-expressing GCaMP6f (green) and PIEZO1-mCherry (red), with a pipette-controlled bead locally touching the cell (grey). **B)** Localized Ca^{2+} influx triggered by tether stretch. Dashed line shows the tether attachment point. Ca^{2+} diffused from the point of entry to gradually fill the cell. There was no evidence of Ca^{2+} entry at any point other than the site of tether attachment. **C)** Sequential tether pulling from two points on the same cell (white arrows). Top: pulling from left edge of the cell. The image at t = 0 shows the expression of PIEZO1-mCherry. Bottom: pulling from the right sides of the same cell. For both tether pulls, Ca^{2+} diffused from the point of entry to gradually fill the cell. There was no evidence of Ca^{2+} entry at any point other than the site of tether attachment. Images in **B** and **C** are composites of mean fluorescence (grey) and changes in fluorescence (heat map). Scale bars in all panels 10 μm.

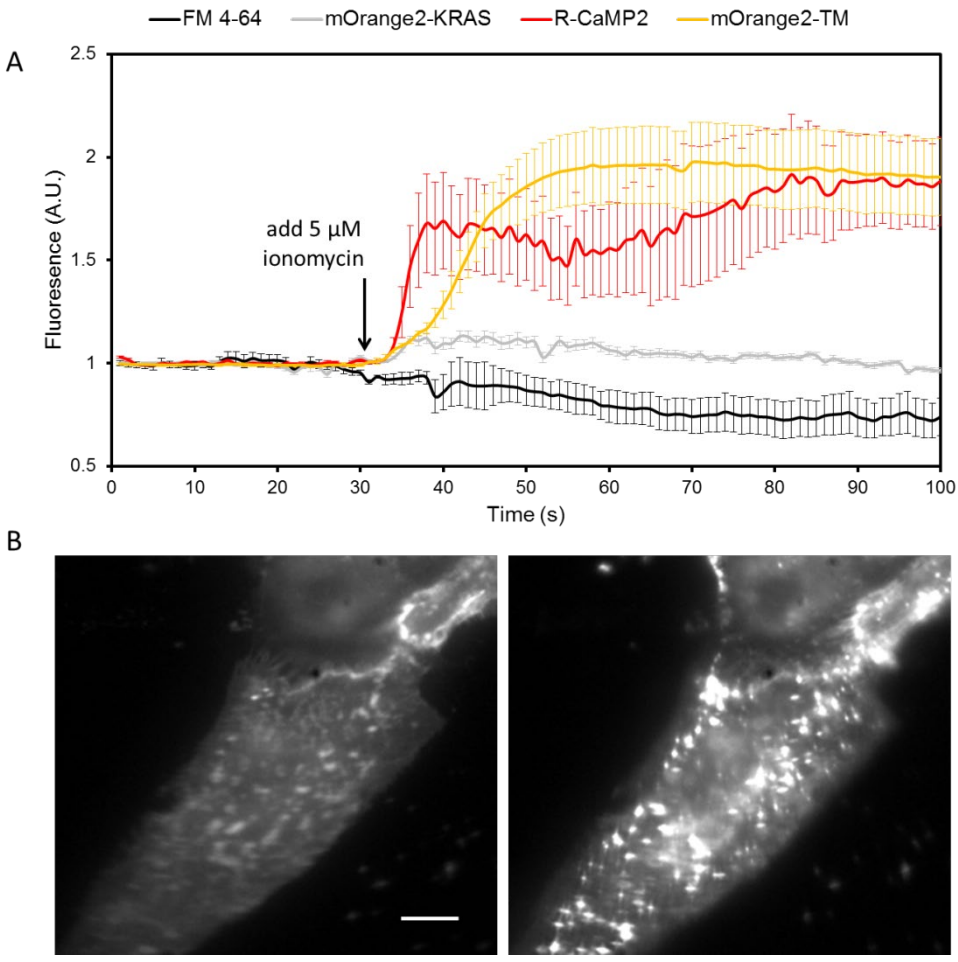

Fig. S11. Validating mOrange2-TM as a vesicle fusion reporter.

A) Validating ionomycin as a means to induce vesicle fusion. In MDCK cells expressing R-CaMP2, ionomycin (5 µM) induced a rapid increase in fluorescence (red, *n* = 4 cells) indicating Ca^{2+} influx. Fresh MDCK cells were incubated with FM 4-64 to load the dye into vesicles and then the dye was washed from the extracellular medium. Ionomycin led to a decrease in fluorescence (black, n = 4 cells), consistent with ionomycin-induced vesicle fusion. In MDCK cells expressing mOrange2-TM, ionomycin induced a rapid increase in fluorescence (orange, n = 7 cells), consistent with vesicle fusion and de-acidification of the vesicles. As a control experiment, ionomycin was added to MDCK cells expressing mOrange2-KRAS, which targeted the fluorescent protein to the inner leaflet of plasma membrane and to the cytoplasmic surface of vesicles. Ionomycin did not affect the fluorescence of these cells (grey, n = 5 cells). Error bars are s.e.m.. **B)** Image of MDCK cells expressing mOrange2-TM before (left) and after (right) adding ionomycin. Scale bar 10 µm.

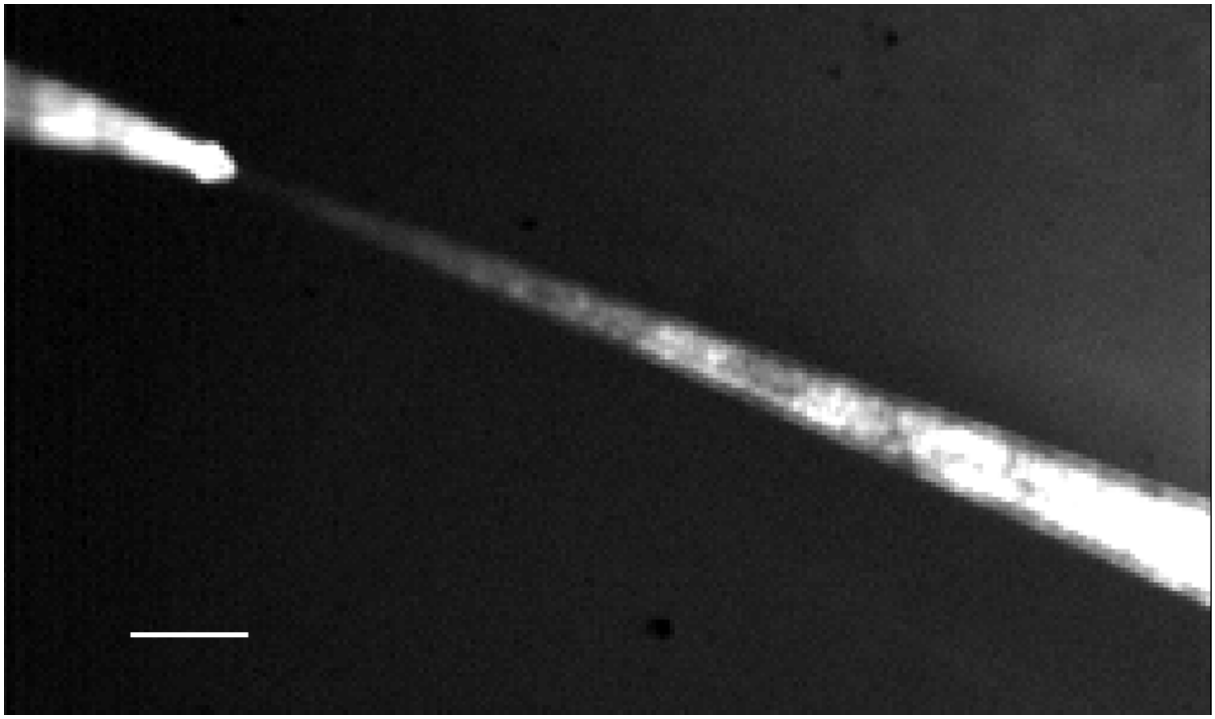

Fig. S12. Tracking the flow profile from the pipette for shear perturbation to cells.
The pipette is on the upper left. The flow was visualized with fluorescent beads. Scale bar 100 μm.

Supplementary Tables

Parameter	Symbol	Value	Reference
Bending stiffness	κ	$(1.9 \pm 0.2) \times 10^{-19}$ J, ~45 k_BT	This work (Dai et al., 1999)
2D viscosity	η	$(3.0 \pm 0.4) \times 10^{-3}$ pN·s/μm	This work, (Bussell et al., 1995; Kusumi et al., 2005)
Stretch modulus	E_m	40 pN/μm	(Hochmuth, 2000; Needham and Hochmuth, 1992)
Obstacle radius	a	2 nm	(Bussell et al., 1995)
Obstacle fill fraction	ϕ_i	10 - 20%	This work.
Tension diffusion coeff.	D_σ	0.024 ± 0.05 μm^2/s	This work, Eq. S11.
Tracer diffusion coeff. in intact cell membrane	D_s	See Supplementary Table S2	This work, (Kusumi et al., 2005)

Table S1. Physical parameters used in this study.

Tracer molecules	D_S^{cell} (μm^2/s)	D_S^{tether} (μm^2/s)	Ratio
DRD2-eGFP	0.037 ± 0.005 (n=10)	0.76 ± 0.08 (n=10)	21 ± 4
CheRiff-eGFP	0.035 ± 0.003 (n=4)	0.48 ± 0.07 (n=4)	14 ± 3
ASAP1	0.024 ± 0.003 (n=4)	0.5 ± 0.15 (n=4)	21 ± 7
eGFP-TM	0.05 ± 0.01 (n=3)	0.81 ± 0.22 (n=3)	16 ± 5
GPI-eGFP	0.10 ± 0.03 (n=3)	1.07 ± 0.05 (n=3)	11 ± 4

Table S2. Diffusion coefficients of different tracer molecules measured on a tether and a cell body with FRAP as described in Fig. S6. All reported values are mean ± s.e.m. See *Materials and Methods* for details of DNA constructs.

Reference List

Brochard-Wyart, F., Borghi, N., Cuvelier, D., and Nassoy, P. (2006). Hydrodynamic narrowing of tubes extruded from cells. Proceedings of the National Academy of Sciences *103,* 7660-7663.

Bussell, S.J., Koch, D.L., and Hammer, D.A. (1995). Effect of hydrodynamic interactions on the diffusion of integral membrane proteins: diffusion in plasma membranes. Biophys. J. *68,* 1836-1849.

Charras, G.T., Yarrow, J.C., Horton, M.A., Mahadevan, L., and Mitchison, T.J. (2005). Non-equilibration of hydrostatic pressure in blebbing cells. Nature *435,* 365-369.

Chen, T., Wardill, T.J., Sun, Y., Pulver, S.R., Renninger, S.L., Baohan, A., Schreiter, E.R., Kerr, R.a., Orger, M.B., Jayaraman, V.*, et al.* (2013). Ultrasensitive fluorescent proteins for imaging neuronal activity.*499,* 295-300.

Clausen, F.P., Colin-York, H., Schneider, F., Eggeling, C., and Fritzsche, M. (2017). Dissecting the actin cortex density and membrane-cortex distance in living cells by super-resolution microscopy. J. Phys. D *50,* 064002.

Dai, H.J., Kong, J., Zhou, C.W., Franklin, N., Tombler, T., Cassell, A., Fan, S.S., and Chapline, M. (1999). Controlled chemical routes to nanotube architectures, physics, and devices. J Phys Chem B *103,* 11246-11255.

Derényi, I., Jülicher, F., and Prost, J. (2002). Formation and Interaction of Membrane Tubes. Phys. Rev. Lett. *88,* 238101.

Domanov, Y.A., Aimon, S., Toombes, G.E.S., Renner, M., Quemeneur, F., Triller, A., Turner, M.S., and Bassereau, P. (2011). Mobility in geometrically confined membranes. Proceedings of the National Academy of Sciences *108,* 12605-12610.

Evans, E., and Rawicz, W. (1990). Entropy-driven tension and bending elasticity in condensed-fluid membranes. Phys. Rev. Lett. *64,* 2094-2097.

Gauthier, N.C., Rossier, O.M., Mathur, A., Hone, J.C., and Sheetz, M.P. (2009). Plasma Membrane Area Increases with Spread Area by Exocytosis of a GPI-anchored Protein Compartment. Mol. Biol. Cell *20,* 3261-3272.

Heinrich, M., Tian, A., Esposito, C., and Baumgart, T. (2010). Dynamic sorting of lipids and proteins in membrane tubes with a moving phase boundary. Proceedings of the National Academy of Sciences *107,* 7208-7213.

Hochmuth, R.M., Mohandas, N., and Blackshear, P.L. (1973). Measurement of the Elastic Modulus for Red Cell Membrane Using a Fluid Mechanical Technique. Biophysical Journal *13,* 747-762.

Hochmuth, R.M. (2000). Micropipette aspiration of living cells. Journal of Biomechanics *33,* 15-22.

Howells, I.D. (1974). Drag due to the motion of a Newtonian fluid through a sparse random array of small fixed rigid objects. Journal of Fluid Mechanics *64,* 449-476.

Inoue, M., Takeuchi, A., Horigane, S., Ohkura, M., Gengyo-Ando, K., Fujii, H., Kamijo, S., Takemoto-Kimura, S., Kano, M., and Nakai, J. (2015). Rational design of a high-affinity, fast, red calcium indicator R-CaMP2. Nature Methods *12,* 64-70.

Jiang, M., and Chen, G. (2006). High Ca^{2+} -phosphate transfection efficiency in low-density neuronal cultures. Nat. Protocols *1,* 695-700.

Kang, M., Day, C.A., Kenworthy, A.K., and DiBenedetto, E. (2012). Simplified Equation to Extract Diffusion Coefficients from Confocal FRAP Data. Traffic *13,* 1589-1600.

Keren, K., Pincus, Z., Allen, G.M., Barnhart, E.L., Marriott, G., Mogilner, A., and Theriot, J.A. (2008). Mechanism of shape determination in motile cells. Nature *453,* 475-480.

Kralj, J.M., Hochbaum, D.R., Douglass, A.D., and Cohen, A.E. (2011). Electrical spiking in Escherichia coli probed with a fluorescent voltage indicating protein. Science *333,* 345-348.

Kusumi, A., Nakada, C., Ritchie, K., Murase, K., Suzuki, K., Murakoshi, H., Kasai, R.S., Kondo, J., and Fujiwara, T. (2005). Paradigm shift of the plasma membrane concept from the two-dimensional continuum fluid to the partitioned fluid: high-speed single-molecule tracking of membrane molecules. Annu. Rev. Biophys. Biomol. Struct. *34,* 351-378.

Needham, D., and Hochmuth, R. (1992). A sensitive measure of surface stress in the resting neutrophil. Biophys. J. *61,* 1664-1670.

Rhee, J.M., Pirity, M.K., Lackan, C.S., Long, J.Z., Kondoh, G., Takeda, J., and Hadjantonakis, A. (2006). In Vivo Imaging and Differential Localization of Lipid-Modified GFP-Variant Fusions in Embryonic Stem Cells and Mice. Genesis (New York, N.Y.: 2000) *44,* 202-218.

Rosholm, K.R., Leijnse, N., Mantsiou, A., Tkach, V., Pedersen, S.L., Wirth, V.F., Oddershede, L.B., Jensen, K.J., Martinez, K.L., Hatzakis, N.S.*, et al.* (2017). Membrane curvature regulates ligand-specific membrane sorting of GPCRs in living cells. Nat Chem Biol *13,* 724-729.

Saffman, P.G., and Delbrück, M. (1975). Brownian motion in biological membranes. Proceedings of the National Academy of Sciences *72,* 3111-3113.

Shen, H., Pirruccello, M., and De Camilli, P. SnapShot: Membrane Curvature Sensors and Generators. Cell *150,* 1300-1300.e2.

Shi, Z., and Baumgart, T. (2015). Membrane tension and peripheral protein density mediate membrane shape transitions. Nature Communications *6,* 5974.

Zeng, B., Chen, G., Garcia-Vaz, E., Bhandari, S., Daskoulidou, N., Berglund, L.M., Jiang, H., Hallett, T., Zhou, L., and Huang, L. (2017). ORAI channels are critical for receptor-mediated endocytosis of albumin. Nature Communications *8,* 1920.